

ARTICLE

Open Access

All-optical observation of giant spin transparency at the topological insulator BiSbTe_{1.5}Se_{1.5}/Co₂₀Fe₆₀B₂₀ interface

Suchetana Mukhopadhyay^{1,2}, Pratap Kumar Pal¹, Subhadeep Manna², Chiranjib Mitra² and Anjan Barman¹

Abstract

The rise of three-dimensional topological insulators as an attractive playground for the observation and control of various spin-orbit effects has ushered in the field of topological spintronics. To fully exploit their potential as efficient spin-orbit torque generators, it is crucial to investigate the efficiency of spin injection and transport at various topological insulator/ferromagnet interfaces, as characterized by their spin-mixing conductances and interfacial spin transparencies. Here, we use all-optical time-resolved magneto-optical Kerr effect magnetometry to demonstrate efficient room-temperature spin pumping in Sub/BiSbTe_{1.5}Se_{1.5}(BSTS)/Co₂₀Fe₆₀B₂₀(CoFeB)/SiO₂ thin films. From the modulation of Gilbert damping with BSTS and CoFeB thicknesses, the spin-mixing conductances of the BSTS/CoFeB interface and the spin diffusion length in BSTS are determined. For BSTS thicknesses far exceeding the spin diffusion length, in the so-called “perfect spin sink” regime, we obtain an interfacial spin transparency as high as 0.9, promoting such systems as scintillating candidates for spin-orbitronic devices.

Introduction

Topological insulators (TIs) are a novel class of quantum materials exhibiting topologically nontrivial band structures and hosting a wide range of exotic spin phenomena that have been a subject of extensive research over the past decade. Essentially, TIs are gapped band insulators in the bulk exhibiting band inversions at specific high-symmetry points in the band structure traversed by linearly dispersive metallic surface states. The surface states in 3D TIs^{1–3} have a Dirac cone character shown by angle-resolved photoemission spectroscopy studies⁴ and are populated by massless Dirac fermions⁵, which enable conduction when the Fermi level resides in the bulk band gap. The presence of band inversions constitutes a key component of the topological phase⁶ and has been variously attributed to strong spin-orbit coupling (SOC), which leads to the opening of gaps in the bulk

band structure⁷, as well as to scalar relativistic effects and lattice strain^{8,9}. Several exotic properties of TIs make them uniquely primed for spintronics applications, exemplified by the helical spin texture and spin-momentum locking exhibited by their surface states. The surface states in TIs are unique in that they are topologically protected by time-reversal symmetry⁷, causing them to be immune to back-scattering. The helical spin polarization of the surface states^{4,10,11} protects surface carriers from spin-independent scattering and localization and promotes long spin coherence lengths desirable for device applications^{7,12}. This hallmark feature is a manifestation of so-called “spin-momentum locking,” wherein the in-plane spin of the surface states is “locked” orthogonal to the direction of electron motion^{13,14}. As a result, spin accumulation can be intrinsically generated when an unpolarized charge current flows in topological surface states, whose orientation and amplitude may be controlled by the charge current^{11,15}. Spin-momentum locking promotes larger nonequilibrium spin accumulation in comparison to the Edelstein effect¹⁶ in the presence of Rashba-type SOC^{17,18}. In addition to the high

Correspondence: Anjan Barman (abarman@bose.res.in)

¹Department of Condensed Matter and Materials Physics, S.N. Bose National Center for Basic Sciences, Block-JD, Sector III, Salt Lake, Kolkata 700106, India

²Department of Physical Sciences, Indian Institute of Science Education and Research, Mohanpur, West Bengal 741252, India

© The Author(s) 2023



Open Access This article is licensed under a Creative Commons Attribution 4.0 International License, which permits use, sharing, adaptation, distribution and reproduction in any medium or format, as long as you give appropriate credit to the original author(s) and the source, provide a link to the Creative Commons license, and indicate if changes were made. The images or other third party material in this article are included in the article's Creative Commons license, unless indicated otherwise in a credit line to the material. If material is not included in the article's Creative Commons license and your intended use is not permitted by statutory regulation or exceeds the permitted use, you will need to obtain permission directly from the copyright holder. To view a copy of this license, visit <http://creativecommons.org/licenses/by/4.0/>.

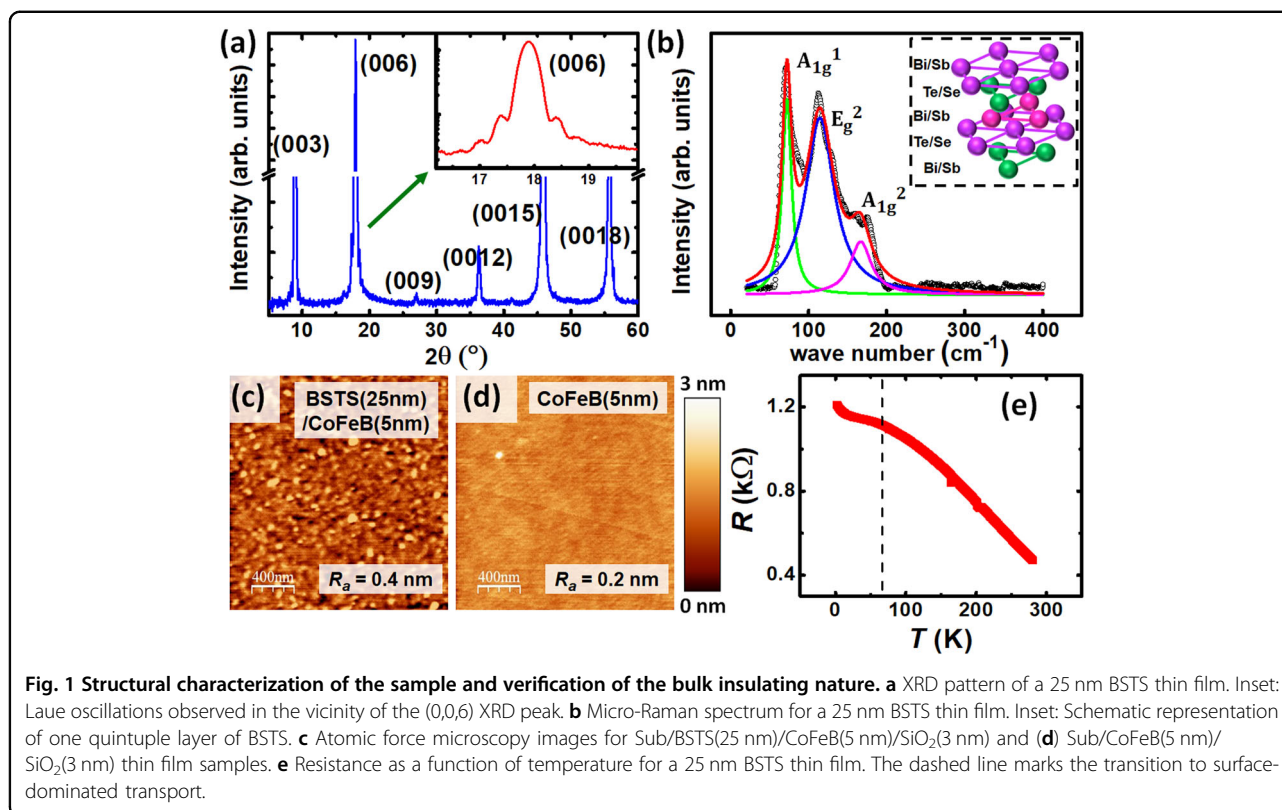
SOC, since the electrical resistivity of the topological insulators is at least an order of magnitude higher than that of most heavy transition metals, these insulators are excellent spin current detectors¹⁹.

In view of their appeal for spintronics and spin-orbitronics, topological insulator/ferromagnet (TI/FM) heterostructures have emerged as a subject of widespread interest. The charge-to-spin conversion efficiency in TIs is projected to be at least an order of magnitude higher than that attainable in heavy metals^{17,20,21}. Several spin-orbit effects are reported in TI/FM systems, such as spin pumping^{17,22}, the spin Hall effect²⁰ and the inverse spin Hall effect of the bulk²³, Rashba²⁴ and inverse Rashba-Edelstein effects and the anomalous Hall effect²⁵. Being free of the impedance mismatch problem, spin pumping provides an effective means to probe spin injection and transport in TIs^{23,26}. Spin angular momentum from the precessing magnetization of an FM is injected or pumped into an adjacent nonmagnet (NM) in the form of pure spin current which manifests as an enhanced damping of magnetization in the FM layer. The efficiency of spin pumping in an NM/FM system is quantified by two parameters characterizing the interface: the spin-mixing conductance²⁷ and the interfacial spin transparency^{28,29}. The spin transparency of an interface controls the amount of spin current that can be transmitted across the interface without reflection or absorption. Identifying and engineering highly transparent interfaces promotes increased efficiency of spin current transfer, which is desirable for applications in spin-torque-based devices³⁰. To date, most reports of spin-to-charge interconversion mechanisms in TI/FM have made use of magnetoresistance measurements^{11,15} or electrical detection of spin injection and transport^{17,22,23} and have focused on second-generation binary TIs, such as Bi₂Se₃, Bi₂Te₃ and Sb₂Te₃. These second-generation TIs are well known to suffer from the presence of parasitic crystalline defects in the bulk, leading to significant bulk conduction in transport measurements^{2,31,32}, which causes the surface states to be difficult to isolate. In 2014, Ando et al.¹⁵ identified the alloy Bi_{2-x}Sb_xTe_{3-y}Se_y to have the lowest defect density and best bulk insulating properties to date. Thus, among the 3D TIs well studied in the literature, the alloy Bi_{2-x}Sb_xTe_{3-y}Se_y is considered to be an exemplary system for achieving the unique properties of TIs due to the tunability of the band structure and transport properties depending on its stoichiometry. For specific stoichiometries, the compensation of p-type carriers due to (Bi, Sb)/Te antisite defects by n-type selenium vacancies can lead to an effective cancellation of bulk carriers^{31,33,34}. Well-defined topological surface states and surface-dominated transport at unprecedented temperatures can be observed in BSTS³⁵⁻³⁷, making it an ideal system for achieving the unique advantages of TIs.

In this work, we report an all-optical investigation of spin pumping in BiSbTe_{1.5}Se_{1.5}(BSTS)/Co₂₀Fe₆₀B₂₀(CoFeB) bilayer thin films with the objective of extracting the spin-mixing conductance and spin transparency of these heterostructures and determining the spin diffusion length in BSTS. To excite and detect the magnetization dynamics in these systems, we use time-resolved magneto-optical Kerr effect (TR-MOKE) magnetometry³⁸, a local and noninvasive pump-probe detection scheme recently proposed to be a viable alternative to the more commonly used electrical techniques for the study of spin pumping in a heavy metal/FM bilayer system²⁹. In contrast to electrical detection techniques, such as spin-torque ferromagnetic resonance (ST-FMR), TR-MOKE bypasses the need for any delicate microfabrication and avoids limiting factors that could be inherently present in those methods, such as large area averaging and inhomogeneous linewidth broadening^{39,40}. The damping can be unambiguously extracted from the decaying amplitude of the oscillatory Kerr signal, free from experimental artifacts arising due to multimodal oscillation and impurity or defect scattering. By studying the modulation of damping as a function of BSTS thickness, we have extracted the intrinsic spin-mixing conductance $G_{\uparrow\downarrow}$ of the BSTS/CoFeB interface and estimated the spin diffusion length λ_s in BSTS. Subsequently, the CoFeB-thickness-dependent modulation of damping was used to extract the effective spin-mixing conductance G_{eff} a quantity that can be derived from $G_{\uparrow\downarrow}$ by including the backflow of the spin angular momentum into the FM. Additionally, the role of two-magnon scattering (TMS) in the modulation of damping in these systems was isolated, and control experiments were performed by inserting a thin copper (Cu) spacer layer of varying thickness between the BSTS and the CoFeB layers to confirm that spin pumping plays the primary role in the thickness-dependent modulation of damping observed in our system. The high efficiency of the observed spin pumping is directly related to the high SOC and the high resistivity of the PLD-grown BSTS topological insulator, highlighting its feasibility as a room-temperature spin current detector.

Results

The crystallinity of the pulsed laser deposition (PLD)-grown BSTS thin films was investigated by X-ray diffraction (XRD) measurements. BSTS crystallizes in a rhombohedral crystal structure with the $R\bar{3}m$ space group³¹. The structure consists of repeated units of five atomic layers stacked along the crystallographic c-axis, otherwise known as the quintuple layers, as illustrated in the inset of Fig. 1b. The XRD pattern of a 25 nm-thick BSTS thin film is shown in Fig. 1a. The XRD peaks were obtained at (0,0,3*n*) indexed as (0,0,3), (0,0,6), (0,0,9), (0,0,12), (0,0,15) and (0,0,18), reflecting the preferred c-axis orientation³¹. The obtained peaks showed an exact match with a PLD-grown BSTS sample of identical stoichiometry reported previously³⁴ as well as with



multiple other reports in BSTS⁴¹ and similarly *c*-axis oriented polycrystalline Bi₂Se₃^{42,43}, Bi₂Te₃⁴⁴ and Bi₂Te_{3-x}Se_x⁴⁵ thin films. Additionally, clear Laue oscillations consistent with the film thickness were observed, as shown in the inset of Fig. 1a close to the (0,0,6) peak, demonstrating the high crystalline quality and uniformity of these films.

Micro-Raman spectroscopy measurements using a Lab Ram HR 800 micro-Raman spectrometer (Horiba France SAS; $\lambda = 533$ nm, objective = 100 \times , grating 1800 lines/mm, spot size 10 μ m) were carried out on the BSTS films to investigate their molecular structure. Five atoms are present in the primitive unit cell of BSTS, producing $(3N-3) = 12$ optical phonon modes. An irreducible representation of $\Gamma_{vib} = 2A_{1g} + 2E_g$ can be derived⁴⁶, where A_{1g} represents out-of-plane and E_g represents in-plane vibrational modes. The Raman spectrum of a 25 nm-thick BSTS film is presented in Fig. 1b, showing three of the four normal modes at 71.6 cm^{-1} , 113.9 cm^{-1} and 166.2 cm^{-1} . Out-of-plane vibrations induce smaller displacements of vibrating atoms, leading to higher phonon frequencies compared to the corresponding in-plane modes^{46,47}. Correspondingly, the three Raman modes in Fig. 1b were designated as the A_{1g}^1 , E_g^2 and A_{1g}^2 modes⁴⁸. These results effectively agreed with previous reports of Raman measurements in PLD-grown BSTS having the same stoichiometry as our films³⁴.

Table 1 Average topographical roughness values obtained from the AFM data analysis.

<i>d</i> (nm)	2	3	4	5	10
R_a [BSTS/CoFeB(<i>d</i>)] (nm)	0.54	0.54	0.48	0.48	0.45
R_a [CoFeB(<i>d</i>)] (nm)	0.20	0.18	0.18	0.18	0.21

The surface topography of the samples was studied using atomic force microscopy (AFM). AFM images of Sub/BSTS(25 nm)/CoFeB(5 nm)/SiO₂(3 nm) and Sub/CoFeB(5 nm)/SiO₂(3 nm) films are shown in Fig. 1c, d. The average topographical roughness (R_a) of the Sub/BSTS(25 nm)/CoFeB(*d*)/SiO₂(3 nm) samples with different thicknesses *d* of the CoFeB layer are listed in Table 1 along with the R_a values of the reference CoFeB films of the corresponding thickness. The R_a value was found to be slightly higher for the bilayers than for the reference films which is not surprising given the PLD growth of the BSTS, which can lead to the granular nature of the film surface⁴⁹. Due to the low thickness of the CoFeB films, the R_a value obtained from AFM analysis bears the signature of the interfacial roughness. In the presence of BSTS, R_a was found to slightly increase with decreasing CoFeB thickness, indicating higher interfacial disorder at lower thicknesses. The R_a values in the reference CoFeB films

were found to be independent of CoFeB thickness. The roughness values negligibly varied in different regions of the same sample, indicating uniform film growth. For all samples, the average topographical roughness was found to be quite low in the sub-nm range.

Figure 1e shows the temperature dependence of the resistance of a 25 nm-thick BSTS thin film. The R - T behavior is characteristic of the bulk insulating nature of BSTS and has been previously reported in BSTS systems⁴⁹. The measured resistance increases with decreasing temperature until approximately 66 K, marked by the dashed line in Fig. 1e. At lower temperatures, a transition to the surface-dominated metallic conduction regime becomes apparent by the sharp change in the curvature and a dip in the measured resistance. This transition can be considered to be a qualitative signature of the weak antilocalization effect in highly insulating topological insulators, such as BSTS^{49,50}, as the metallicity of the topological protected surface states became apparent even at temperatures as high as 66 K. On the other hand, the small upturn in the R - T curve at even lower temperatures ≤ 14 K can be attributed to the freezing of the bulk carriers.

Enhancement of Gilbert damping due to spin pumping

The magnetization dynamics of a ferromagnetic system in the presence of a magnetic field consists of the Landau-Lifshitz torque and the intrinsic Gilbert damping; the Landau-Lifshitz torque leads to the precession of the magnetization direction around the effective magnetic field direction, and the intrinsic Gilbert damping results in the precessional oscillations steadily diminishing in amplitude until an equilibrium time-independent magnetization direction is attained. In addition to the local material-specific Gilbert damping, nonlocal effects occur when an FM layer is placed adjacent to certain NM materials, which can lead to an enhancement of the effective damping. Tserkovnyak et al. in 2002⁵¹ proposed one such mechanism the so-called “spin-pumping” effect, in which the precessing magnetization in the FM pumps angular momentum into the adjacent NM layer, thus losing energy and hence damping out more rapidly^{51–53}. The overall dynamics of the magnetization vector can be theoretically described by a modified version of the Landau-Lifshitz-Gilbert equation, given by the following:

$$\frac{dm}{dt} = -\gamma(\mathbf{m}H_{\text{eff}}) + \alpha_0 \left(\mathbf{m} \frac{dm}{dt} \right) + \frac{\gamma}{VM_s} I_0 \quad (1)$$

where γ is the gyromagnetic ratio, α_0 is the intrinsic Gilbert damping, H_{eff} is the effective magnetic field, V is the volume of the FM and M_s is the saturation magnetization. The total pumped current I_0 consists of the DC charge current I_{dc} (zero in our case), the spin

current I_s^{pump} pumped into the NM layer and the backflow current I_s^{back} , that returns back into the FM:

$$I_0 = I_{dc} + I_s^{\text{pump}} + I_s^{\text{back}} \quad (2)$$

The resultant flow of angular momentum across the NM/FM interface depends on the relative balance between the forward and backflow currents. The forward current depends on the intrinsic spin-mixing conductance $G_{\uparrow\downarrow}$ ²⁷, which acts as a measure of the spin transfer across it. Under the ballistic approximation valid for film thicknesses less than the momentum mean free path⁵⁴, $G_{\uparrow\downarrow}$ can be extracted from the variation of the effective Gilbert damping α_{eff} with the thickness t of the NM layer using the following relationship^{54,55}:

$$\alpha_{\text{eff}} = \alpha_0 + \frac{g\mu_B G_{\uparrow\downarrow}}{4\pi M_s d} \left(1 - e^{-\frac{2t}{\lambda_s}} \right) \quad (3)$$

where d is the thickness of the FM layer and λ_s is the spin diffusion length in the NM. On the other hand, spin current backflow occurs primarily due to spin accumulation at the interface, which reduces the efficiency of spin transfer. The spin accumulation can be quantified by the backflow factor β :

$$\beta = \left(G_{\uparrow\downarrow} \sqrt{\frac{4\epsilon}{3}} \tanh\left(\frac{t}{\lambda_s}\right) \right)^{-1} \quad (4)$$

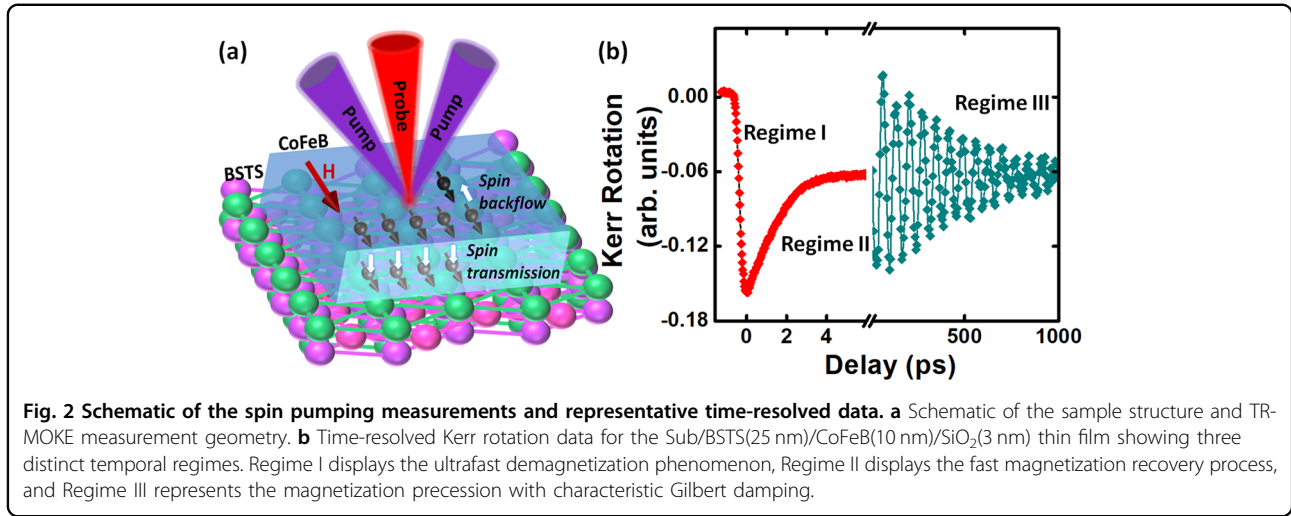
where ϵ is the spin-flip scattering probability, a material-specific parameter given by^{55,56}:

$$\epsilon = \left(\frac{ze^2}{c} \right)^4 = (z\alpha_{\text{fine}})^4 \quad (5)$$

where $\alpha_{\text{fine}} = 1/137$ is the fine structure constant and z is the atomic number of the NM. The magnitude of ϵ is larger for heavier elements and does not allow the backflow effect to vanish even when the ratio $t/\lambda_s \gg 1$. However, the intrinsic spin-mixing conductance $G_{\uparrow\downarrow}$ is a direct measure of the pure spin current transfer and does not consider the spin backflow. For diffusive spin transport, another quantity, the effective spin-mixing conductance G_{eff} , can be derived from $G_{\uparrow\downarrow}$ by including the backflow factor as⁵³:

$$\begin{aligned} \frac{1}{G_{\text{eff}}} &= \frac{1}{G_{\uparrow\downarrow}} + \beta \\ \Rightarrow G_{\text{eff}} &= \frac{G_{\uparrow\downarrow}}{\left[\sqrt{\frac{4\epsilon}{3}} \tanh\left(\frac{t}{\lambda_s}\right) \right]^{-1} + 1} \end{aligned} \quad (6)$$

Inclusion of the backflow factor causes G_{eff} to be element-dependent and dependent on the thickness of the NM layer. G_{eff} can also be experimentally determined by



studying the dependence of the damping on the FM layer thickness d ^{39,53}.

$$\begin{aligned} \alpha_{eff} &= \alpha_0 + \frac{g\mu_B}{4\pi M_s d} G_{eff} \\ &= \alpha_0 + \frac{g\mu_B}{4\pi M_s d} \frac{G_{\uparrow\downarrow}}{\left[\sqrt{\frac{4\epsilon}{3}} \tanh\left(\frac{t}{\lambda_s}\right)\right]^{-1} + 1} \end{aligned} \quad (7)$$

The latter half of the above equation, derived by substitution of the result in Eq. (6), can be used in the diffusive approximation to model the NM layer thickness dependence of spin pumping for a fixed FM layer thickness d .

In addition to the spin pumping effect, the magnetic disorder and intermixing at an NM/FM interface can lead to loss of spin information and a corresponding decrease in the spin transmission efficiency in the presence of certain interfacial effects other than spin pumping. One such effect is known as spin memory loss (SML), in which interfacial SOC mediates spin-flip scattering events at the interface, leading to reduced spin transmission to the NM^{57,58}. Further losses can occur owing to the TMS effect occurring in the presence of defects and inhomogeneities at the interface^{59,60}, leading to the dephasing of the uniform FMR mode and its scattering into degenerate magnons. The presence of SML or TMS can lead to a larger modulation of effective damping than that arising from pure spin pumping. However, while the modulation due to SML scales inversely with FM thickness similar to spin pumping, that due to TMS scales quadratically, making it possible to straightforwardly isolate its contribution from FM-thickness-dependent measurements of the damping. The total damping modulation arising due to the combined effect of spin pumping and TMS can be

expressed as^{61,62}:

$$\Delta\alpha = \alpha_{eff} - \alpha_0 = \frac{g\mu_B}{4\pi M_s d} G_{eff} + \beta_{TMS} d^{-2} \quad (8)$$

The effect of all these interfacial effects is included in a parameter known as the interfacial spin transparency T which is given by^{28,63}:

$$T = \frac{G_{eff} \tanh\left(\frac{t}{2\lambda_s}\right)}{G_{eff} \coth\left(\frac{t}{\lambda_s}\right) + \frac{h}{2\rho\lambda_s e^2}} \quad (9)$$

The interfacial spin transparency is directly correlated to its effective spin-mixing conductance G_{eff} and regulates the flow of the spin angular momentum across the NM/FM interface. Differences in spin transparency can account for the disparities in the measured spin-Hall angle independent of the SML effect²⁸. Identifying and engineering highly transparent interfaces for efficient spin transfer is crucial for device applications.

All-optical measurement of damping parameter

TR-MOKE magnetometry was used for all-optical probing of magnetization dynamics in the Sub/BSTS(t)/CoFeB(d)/SiO₂(3 nm) samples. A two-color setup with a noncollinear pump-probe geometry was used⁴⁰, as shown in Fig. 2a. Typical time-resolved Kerr rotation data showing different temporal regimes of laser-induced magnetization dynamics are provided in Fig. 2b. Regime I displays the ultrafast demagnetization phenomenon in which laser excitation leads to an ultrafast quenching of magnetization at the picosecond timescale⁶⁴. Regime II displays the fast magnetization recovery process, while the oscillatory Kerr signal of Regime III represents the magnetization precession with the characteristic Gilbert damping, superposed

on a background signal arising from slow relaxation occurring via heat dissipation into the substrate.

To extract the Gilbert damping parameter α_{eff} , the background-subtracted oscillatory Kerr signal is first fitted with a damped sinusoidal function

$$M(t) = M(0)e^{-\frac{t}{\tau}} \sin(2\pi f_{FFT}t + \phi) \quad (10)$$

where f_{FFT} is the precessional frequency, τ is the relaxation time, and ϕ is the initial phase of precession. To extract the effective saturation magnetization M_{eff} of the samples, the bias magnetic field dependence of f_{FFT} is fitted to the Kittel formula relevant for ferromagnetic systems⁶⁵:

$$f_{FFT} = \frac{\gamma_0}{2\pi} \sqrt{H(H + 4\pi M_{eff})} \quad (11)$$

where $\gamma_0 = g\mu_B/\hbar$ is the gyromagnetic ratio and H is the bias magnetic field. From the Kittel fit for the Sub/BSTS(25 nm)/CoFeB(d)/SiO₂(3 nm) samples, M_{eff} decreased with CoFeB thickness d , showing a linear dependence with $1/d$. From a linear fit with the conventional relationship of $M_{eff} = M_s - 2K_s/(4\pi M_s d)$, the saturation magnetization M_s was extracted from the intercept and the interfacial anisotropy K_s was extracted from the slope, as shown in Fig. S1 of the Supplementary Information. K_s serves as an indicator of the strength of the interfacial SOC⁶¹. The value of M_s was found to decrease from 1465 ± 43 emu/cc in the reference CoFeB films to 1324 ± 27 emu/cc in the BSTS/CoFeB bilayers, while K_s slightly increased from 0.962 ± 0.0269 erg/cm² in the reference films to 0.988 ± 0.0283 erg/cm² in the bilayers. The reduction in M_s in the TI/FM bilayers could potentially originate from the magnetic proximity effect at the BSTS/CoFeB interface, in which orbital hybridization between the $3d$ electrons in CoFe and the topological surface states of BSTS could introduce a perpendicular magnetic anisotropy manifested as a reduced M_s ^{66,67} at low temperatures. However, under ambient conditions, a more likely cause is the presence of some degree of atomic intermixing at the BSTS/CoFeB interface^{68,69}. Finally, the effective Gilbert damping parameter α_{eff} is calculated using the extracted values of τ and M_{eff} as follows:

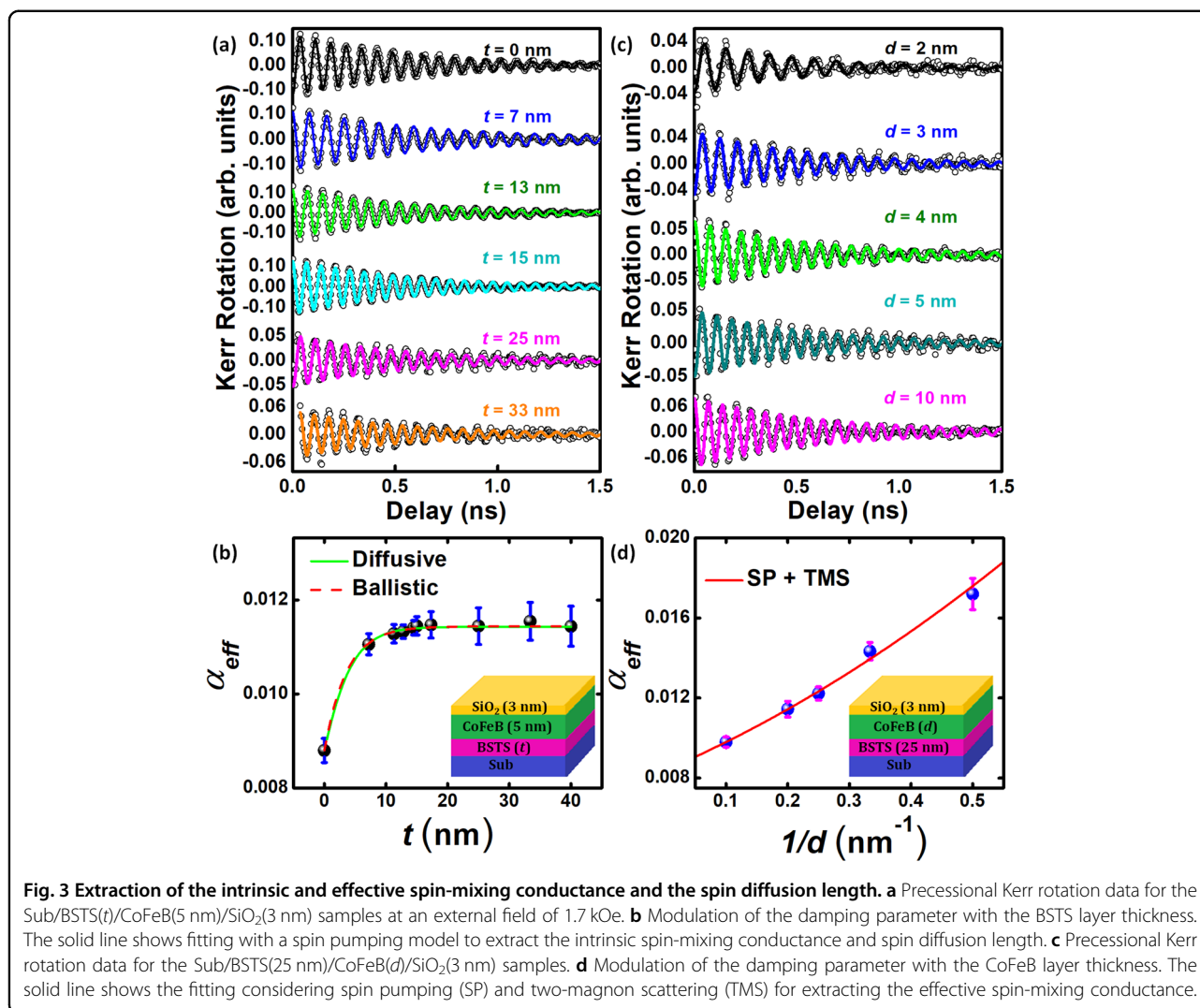
$$\alpha_{eff} = \frac{1}{\gamma_0 \tau (H + 2\pi M_{eff})} \quad (12)$$

Details of the bias-field dependent TR-MOKE measurements are provided in Section I of the Supplementary Information.

Thickness-dependent modulation of damping

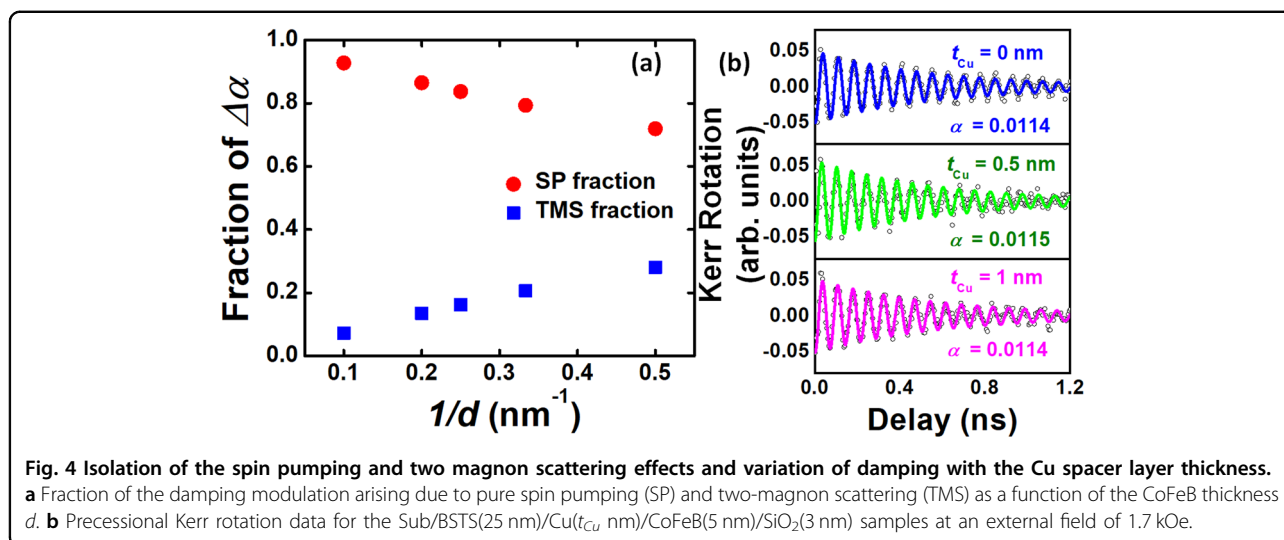
The background-subtracted precessional Kerr rotation data taken in the presence of an ~ 1.7 kOe saturating magnetic field for the Sub/BSTS(t)/CoFeB(5 nm)/SiO₂(3 nm) sample are given in Fig. 3a, where t was varied from 7 to 40 nm. The lowest thickness of the BSTS

studied in our experiments was well above twice the approximate surface state thickness^{70,71} to eliminate the possibility of a crossover from the topological phase to a trivial gapped insulator, which may occur due to quantum tunnelling between opposite surfaces if the thickness is reduced below a critical limit⁷⁰. In the absence of the BSTS underlayer, the damping of 5 nm CoFeB was found to be 0.0084, which was considered the intrinsic Gilbert damping α_0 . As shown in Fig. 3b, the effective damping in the presence of the BSTS underlayer was found to show a nonmonotonic variation consisting of a sharp enhancement in α_{eff} from its intrinsic value of 0.0084 to a saturating value of 0.0114 at high values of t . The observed dependence is a characteristic signature of spin pumping, showing a similar nature to those reported in various systems involving ferromagnetic thin films interfaced with a topologically trivial NM^{29,30,62}. However, this dependence is not immediately expected in topological systems where the spin-to-charge conversion efficiency in several spin pumping experiments has been attributed to a dominant role played by the topologically protected surface states^{23,72}, whose thicknesses do not vary with the film thickness. In topological insulators, the SOC strength is expected to be different in the surface states versus the bulk and spin pumping also contributes to the inverse Edelstein effect (IEE) in the spin-momentum-locked topological surface states. The pumped spin current from the ferromagnet results in a spin imbalance in the surface state, whereafter the spin-momentum locking results in the generation of a charge current J_c confined to two dimensions²². This mechanism is distinct from the ISHE, where a spin current flowing within the bulk of the material is converted into a 3D charge current. However, in room-temperature spin-pumping experiments it is very difficult to distinguish the ISHE and the IEE of the surface state, and moreover ISHE is found to dominate over the latter¹⁷. Although it has been reported previously that the SOC of the topological surface states could enhance the pure spin current injected into the TI¹⁷, any contribution of the surface states to the spin pumping should be uniform over the entire experimental thickness range, and cannot explain on its own the variation in Fig. 3b. We concluded that in our case, the experimentally observed variation in α_{eff} with BSTS thickness was likely caused as a consequence of strong bulk spin-orbit coupling of the heavy metallic bismuth-based alloy, analogous to a normal heavy metal. Since all measurements were carried out under ambient conditions, this observation could indicate the presence of surface-to-bulk scattering at room temperature, leading to the scattering of injected carriers into the bulk⁴⁹. Studying the modulation of α_{eff} as a function of temperature could elucidate the precise contribution of the surface states to the spin pumping effect; in particular, by lowering the temperature to traverse the inflection



point at 66 K in the R-T characteristics which signals the emergence of surface-dominated transport. Such an investigation necessitates temperature-dependent TR-MOKE or FMR measurements of the damping modulation in the system, which will be a topic of our future research. Fitting the dependence in Fig. 3b with the latter half of Eq. (7), we extracted a value $(4.02 \pm 0.995) \times 10^{15} \text{ cm}^{-2}$ for the intrinsic spin-mixing conductance $G_{\uparrow\downarrow}$. The spin diffusion length was simultaneously obtained from the fit as $\lambda_s = 6.3 \text{ nm}$. The high value of $G_{\uparrow\downarrow}$ and the nonmonotonic change in the damping parameter both indicate spin current injection into the BSTS. For completeness, we also fitted the data in Fig. 3b using the ballistic transport model of Eq. (3), obtaining $G_{\uparrow\downarrow} = (1.19 \pm 0.006) \times 10^{15} \text{ cm}^{-2}$ and $\lambda_s = 7.2 \text{ nm}$. Using Eq. (5), the spin-flip probability ϵ in these heterostructures was calculated to be 13.4%. This high value of $\epsilon \gg 1.0 \times 10^{-2}$ was a direct manifestation of strong spin-orbit coupling of heavy metallic Bi, which

makes the Bi-based alloy a good spin sink^{52,53}. Using $\epsilon = 0.134$ and the values of $G_{\uparrow\downarrow}$ and λ_s extracted from the fit using Eq. (7), the spin backflow factor β was calculated to be $5.9 \times 10^{-16} \text{ cm}^2$ for the 25 nm-thick BSTS layer. Based on the form of Eq. (4), β is higher for lower thicknesses and asymptotically approaches its lower limit when $t \gg \lambda_s$. However, even at very high thicknesses, β does not reduce to zero due to the finite contribution of the material-dependent quantity ϵ . On the other hand, the exponential form for the backflow factor implicit in Eq. (3) is applicable in the ballistic limit when the thickness of the film is less than the mean free path⁵⁴. The effective spin-mixing conductance G_{eff} includes the presence of the spin backflow and was determined using Eq. (6) to be $(1.19 \pm 0.295) \times 10^{15} \text{ cm}^{-2}$ for $t = 25 \text{ nm}$, approximately a factor of three smaller than $G_{\uparrow\downarrow}$. The inclusion of a nonnegligible spin backflow led to a larger value of $G_{\uparrow\downarrow}$ relative to G_{eff} derived using spin diffusion theory compared to the estimate using the ballistic model.



The variation of G_{eff} calculated in this manner for different thicknesses of BSTS are shown in Fig. S2 of the Supplementary Information.

We next aimed to determine the value of the effective spin-mixing conductance G_{eff} directly from experiment by modeling the FM layer thickness-dependent damping modulation. For this purpose, we chose a BSTS thickness of 25 nm $\gg \lambda_s$, where the BSTS-thickness dependence of the damping saturates such that the effect of varying the CoFeB layer thickness could be eliminated. The precessional data taken at a 1.7 kOe saturating magnetic field for the Sub/BSTS(25 nm)/CoFeB(d)/SiO₂(3 nm) samples are given in Fig. 3 (c), where d was varied from 2 to 10 nm. The damping was found to show a sharp increase with the inverse of the CoFeB layer thickness, consistent with the presence of a strong spin pumping effect in our systems. The observed dependence was fitted with the sum of linear and quadratic scaling with the inverse of CoFeB thickness provided in Eq. (8), arising from spin pumping and two-magnon scattering effects, respectively. From the fit, the values of effective spin-mixing conductance G_{eff} and β_{TMS} were found to be $(1.19 \pm 0.034) \times 10^{15} \text{ cm}^{-2}$ and $(1.03 \pm 0.116) \times 10^{-16} \text{ cm}^2$, respectively, while the intrinsic Gilbert damping α_0 was found to be 0.0084. Subsequently, the spin pumping and TMS contributions to the total damping modulation from its intrinsic value were isolated using Eq. (8). The TMS contribution was found to increase with decreasing CoFeB thickness, consistent with the higher average roughness values at lower film thickness, as determined from the AFM measurements (Table 1). The finite β_{TMS} value present in these heterostructures is not surprising due to the PLD growth of BSTS. Improving the structural quality of the interface should lead to more efficient spin transmission and a lower percentage of TMS. Regardless, as shown in Fig. 4a, spin pumping emerged as the dominant mechanism

underlying the damping modulation in our case, even at the lowest CoFeB thickness studied.

With the experimentally obtained $G_{\uparrow\downarrow}$ and G_{eff} , the interfacial spin transparency T of the BSTS/CoFeB interface was investigated. T shows a complex dependence on the spin-mixing conductance of an NM/FM interface as well as the spin diffusion length and resistivity of the NM layer. In the spin-Hall magnetoresistance framework, the finite thickness of the BSTS layer was taken into account⁶³. Using the experimentally determined value of $G_{eff} = (1.19 \pm 0.034) \times 10^{15} \text{ cm}^{-2}$ and the extracted values of the resistivity (Section III of the Supplementary Information) and the spin diffusion length $\lambda_s = 6.3 \text{ nm}$, T was calculated from Eq. (9) to be a very high value of 0.9 in the so-called “perfect spin-sink” regime $t \gg \lambda_s$ when the BSTS thickness dependence of the damping modulation saturates⁵⁴, leading to a high effective spin-mixing conductance of the BSTS/CoFeB interface. Thus, high values of T are attainable in BSTS/FM systems, which provides another dimension to their applicability for pure spin-current-based spintronic devices^{30,62}. The strong bulk SOC of the BSTS topological insulator allows easier spin current dissipation⁵², resulting in a high G_{eff} value and a high interfacial spin transparency. In addition to the bulk SOC, the pumped spin current is greatly enhanced by the SOC of the surface¹⁷ which can contribute to the high value of G_{eff} . In addition to high G_{eff} , the high resistivity of BSTS also plays a role in enhancing the interface transparency. Appropriate choice of thickness and exploring the tunability of resistivity in these systems are key to identifying optimal conditions for maximizing the efficiency of spin transfer; these aspects need further exploration and will form the basis of future work.

Finally, a thin Cu spacer layer was introduced between the BSTS and CoFeB layers, and TR-MOKE

measurements were performed as a control experiment. Cu has a small spin-orbit coupling, and hence, very little spin-flip scattering is expected at the Cu interfaces. At the same time, a long spin diffusion length in Cu implies that pure spin current generated by spin pumping can penetrate fully through the spacer. Time-resolved Kerr rotation data for the Sub/BSTS (25 nm)/Cu (t_{Cu})/CoFeB (5 nm)/SiO₂ (3 nm) thin films with $0 \leq t_{Cu} \leq 1$ nm are presented in Fig. 4b. Negligible modulation of damping with the introduction and variation of the Cu spacer thus ruled out the presence of any significant SML effect in our heterostructures and established the dominance of spin pumping in the observed thickness-dependent damping modulation.

Discussion

We used an all-optical time-resolved magneto-optical Kerr effect technique to reveal a sizeable spin pumping effect and interfacial spin transparency in BiSbTe_{1.5}Se_{1.5} (BSTS)/Co₂₀Fe₆₀B₂₀(CoFeB) heterostructures. High-quality BSTS thin films were grown by pulsed laser deposition, which showed characteristic structural features and a typical bulk insulating character with resistance vs. temperature characteristics showing a signature of surface-dominated transport at temperatures as high as 66 K. The modulation of Gilbert damping with the thickness of the CoFeB layer and that of the BSTS underlayer were found to be indicative of an efficient spin pumping effect in these heterostructures, which were characterized by analyzing the variation in Gilbert damping with the respective thicknesses of the BSTS and CoFeB layers. We determined the intrinsic spin-mixing conductance $G_{\uparrow\downarrow}$ of the interface to be $(4.02 \pm 0.995) \times 10^{15} \text{ cm}^{-2}$ and found the spin-diffusion length λ_s in BSTS to be 6.3 nm at room temperature, thus demonstrating optical detection of pure spin current injection into the BSTS layer. Analyzing the CoFeB-thickness-dependent variation in Gilbert damping, we found the effective spin-mixing conductance G_{eff} to be $(1.19 \pm 0.034) \times 10^{15} \text{ cm}^{-2}$ and isolated the two-magnon scattering parameter β_{TMS} , which was calculated to be $(1.03 \pm 0.116) \times 10^{-16} \text{ cm}^2$, thereby revealing spin pumping to be the dominant contributor to the damping modulation. The roles of other interfacial losses, such as spin memory loss, were found to be negligible in comparison to spin pumping in our heterostructures, as evidenced by the negligible modulation of damping upon insertion of a Cu spacer layer at the BSTS/CoFeB interface. Finally, we calculated the interfacial spin transparency T , which we found to be as high as ~ 0.9 (90%) in our heterostructures for a BSTS thickness of 25 nm. High interfacial spin transparency is imperative for the enhanced efficiency of spin transport, and the nearly ideal value we obtained in the BSTS/CoFeB heterostructures are of direct relevance for spin-orbitronic device applications. Our first demonstration of room-temperature spin injection in a highly resistive topological insulator could be useful for future

studies involving the correlation of the spin pumping effect with the interesting properties of topological insulators in general; such as different spin-orbit coupling of surface and bulk, nonmonotonic variation of the resistivity with temperature, thickness-dependent phase transition from the topological to trivial insulating character, and the properties of BSTS in particular, such as high resistivity and tunable band structure by stoichiometry variation. Exploration of the effects of the resistivity and thickness of the topological insulator on the spin diffusion length, spin-mixing conductance and interfacial spin transparency, particularly as the thickness is sufficiently lowered to destroy the surface states and hence isolate the surface state contribution, will be important to identify optimal conditions for maximizing pure spin current transfer in next-generation topological spintronic devices.

Methods

Sample fabrication

Thin films of BSTS topological insulator were grown on SiO₂-coated Si substrates using a pulsed laser deposition technique, wherein BSTS targets of nominal stoichiometry were ablated using a high-powered KrF excimer laser (Coherent Inc.) and deposited on an insulating Si (100) substrate coated with 300-nm-thick SiO₂. Although films deposited by molecular beam epitaxy (MBE) are more frequently used in fundamental research, MBE is a time-consuming and expensive process presenting serious roadblocks for the integration with practical applications; additionally, the growth of Bi_{2-x}Sb_xTe_{3-y}Se_y topological insulators of controllable stoichiometry was not achieved by MBE⁴¹. However, we note that the topology of the surface states are protected irrespective of the lack of epitaxy, as the Dirac electrons propagate in the surface with a topological protection against any nonmagnetic defects, including grain boundaries. The sample thickness was controlled by monitoring the number of laser pulses used to ablate the target once the pulse energy, deposition pressure and substrate-to-target distance were fixed to optimize the plasma plume. Prior to the deposition, the chamber was evacuated to a base pressure of 3×10^{-5} Torr. Deposition was performed in a flowing argon (Ar) environment with an Ar pressure of 3.6×10^{-1} Torr at a substrate temperature of 240 °C. After deposition, the samples were annealed in an Ar atmosphere for 20 min, which aids in mobilizing the Se and Te atoms to their preferred low energy positions within the quintuple layers, greatly reducing residual bulk carriers⁴⁹. The presence of Laue oscillations corresponding to the film thickness in the XRD pattern was testament to the high quality of PLD-grown polycrystalline samples, which was achieved by careful temperature control and use of an optimized in situ annealing temperature during the deposition process.

Subsequently, ferromagnetic CoFeB layers of different thicknesses were grown on top of the PLD-deposited

BSTS by DC magnetron sputtering, followed by deposition of a 3-nm-thick protective capping layer of SiO₂ by RF sputtering to protect it under ambient conditions and prevent it from damages due to high-power laser exposure during optical pump-probe measurements. CoFeB was deposited with a DC voltage of ~375 V, and SiO₂ was deposited with an RF power of 50 W. For the Sub/BSTS (25 nm)/Cu (*t_{Cu}*)/CoFeB (5 nm)/SiO₂ (3 nm) samples, the Cu-spacer layer was deposited at a DC voltage of ~340 V. All depositions were performed at 0.5 mTorr Ar pressure with a base pressure of 1.4×10^{-6} Torr. The deposition conditions were carefully optimized and identical for all the samples. A very low deposition rate of 0.2 Å/s was maintained for the deposition of all metallic films, and 0.1 Å/s for the SiO₂ capping layer in order to achieve uniform deposition down to thicknesses ≤ 1 nm.

TR-MOKE measurements

Measurement of magnetization dynamics in all the thin film samples was carried out using a two-color TR-MOKE technique with a 400 nm pump beam and 800 nm probe beam with a pump-probe cross-correlation width of ~100 fs⁴⁰. This all-optical technique facilitates the direct observation of the precessional oscillations in the pico- and nanosecond time domain. An amplified laser system (Libra, Coherent Inc.) employing a chirped-pulse regenerative amplification technique generates femtosecond laser pulses. The second harmonic of the amplified laser output (wavelength = 400 nm, pulse width > 40 fs, repetition rate = 1 kHz) was used for laser excitation of the ferromagnetic thin films. Meanwhile, the time-delayed fundamental beam (wavelength = 800 nm, pulse width = 40 fs, repetition rate = 1 kHz) was used to probe the ensuing magnetization dynamics. The delay time between the pump and probe pulses was externally controlled by a variable delay generator. A noncollinear pump-probe geometry was adopted in which the pump beam was focused to a spot size of 300 μm and was directed to be obliquely incident on the sample while the probe beam, with a spot size of 100 μm, was incident normal to the sample surface and carefully aligned to the center of the pump spot to detect the local magnetization changes from a uniformly irradiated part of the sample. The pump fluence was set to 10 mJ/cm² and the probe fluence was set to 1 mJ/cm² for all the measurements. Initially, the 800 nm probe beam was orthogonally polarized to the pump. After reflection from the sample surface, the Kerr-rotated probe beam was directed into a Si photodiode after passing through a Glan-Thompson polarizer adjusted to a small angle from extinction to minimize optical artifacts in the Kerr rotation signal. Digital signal processing lock-in amplifiers (Stanford Research Systems, SR830) provided phase-sensitive detection of the modulated signal. The reference signal for lock-in detection was provided by an optical chopper operating at 373 Hz placed in the pump path. All measurements were performed under a 1.7 kOe bias field

applied at a 10°–15° tilt from the sample plane to saturate the magnetization of the samples. All experiments were carried out under ambient temperature and pressure conditions.

Acknowledgements

A.B. gratefully acknowledges financial assistance from the S. N. Bose National Centre for Basic Sciences (SNBNCBS), India under Project Nos. SNB/AB/11-12/96 and SNB/AB/18-19/211 and the Department of Science and Technology (DST), Govt. of India (Grant No. DST/NM/TUE/QM-3/2019-1C-SNB). S.Mukhopadhyay acknowledges DST for the INSPIRE Fellowship. P.K.P. and S.Manna acknowledge the Council of Scientific and Industrial Research (CSIR), India for Senior Research Fellowship. C.M. acknowledges the Science and Engineering Research Board (SERB) (Grant No. EMR/2016/007950) and Department of Science and Technology (DST), Govt. of India (Grant No. DST/ICPS/Quest/2019/22) for financial support.

Author contributions

A.B. and C.M. planned and supervised the project. S.Mukhopadhyay and P.K.P. prepared the samples in consultation with S.Manna; S.Mukhopadhyay performed the optical pump-probe measurements. S.Manna performed the resistivity measurements. S.Mukhopadhyay analyzed the pump-probe data in consultation with A.B. and wrote the original draft. S.Mukhopadhyay and A.B. finalized the manuscript in consultation with all coauthors.

Funding

S. N. Bose National Centre for Basic Sciences (SNBNCBS), India Project SNB/AB/11-12/96 (A.B.). S. N. Bose National Centre for Basic Sciences (SNBNCBS), India Project SNB/AB/18-19/211 (A.B.). Department of Science and Technology (DST), Govt. of India Grant No. DST/NM/TUE/QM-3/2019-1C-SNB (A.B.). Science and Engineering Research Board (SERB) Grant No. EMR/2016/007950 (C.M.). Department of Science and Technology (DST), Govt. of India Grant No. DST/ICPS/Quest/2019/22 (C.M.).

Competing interests

The authors declare no competing interests.

Publisher's note

Springer Nature remains neutral with regard to jurisdictional claims in published maps and institutional affiliations.

Supplementary information The online version contains supplementary material available at <https://doi.org/10.1038/s41427-023-00504-w>.

Received: 31 January 2023 Revised: 10 August 2023 Accepted: 24 August 2023.

Published online: 20 October 2023

References

1. Fu, L., Kane, C. L. & Mele, E. J. Topological insulators in three dimensions. *Phys. Rev. Lett.* **98**, 106803 (2007).
2. Hasan, M. Z. & Kane, C. L. Colloquium: topological insulators. *Rev. Mod. Phys.* **82**, 3045–3067 (2010).
3. Qi, X.-L. & Zhang, S.-C. Topological insulators and superconductors. *Rev. Mod. Phys.* **83**, 1057–1110 (2011).
4. Hsieh, D. et al. A tunable topological insulator in the spin helical Dirac transport regime. *Nature* **460**, 1101–1105 (2009).
5. Chen, C. et al. Tunable Dirac fermion dynamics in topological insulators. *Sci. Rep.* **3**, 2411 (2013).
6. Fu, L. & Kane, C. L. Topological insulators with inversion symmetry. *Phys. Rev. B* **76**, 045302 (2007).
7. Zhang, H. et al. Topological insulators in Bi₂Se₃, Bi₂Te₃ and Sb₂Te₃ with a single Dirac cone on the surface. *Nat. Phys.* **5**, 438–442 (2009).
8. Zhu, Z., Cheng, Y. & Schwingenschlögl, U. Band inversion mechanism in topological insulators: A guideline for materials design. *Phys. Rev. B* **85**, 235401 (2012).
9. Chege, S., Ning'i, P., Sifuna, J. & Amolo, G. O. Origin of band inversion in topological Bi₂Se₃. *AIP Adv.* **10**, 095018 (2020).

10. Nishide, A. et al. Direct mapping of the spin-filtered surface bands of a three-dimensional quantum spin Hall insulator. *Phys. Rev. B* **81**, 041309 (2010).
11. Li, C. H. et al. Electrical detection of charge-current-induced spin polarization due to spin-momentum locking in Bi_2Se_3 . *Nat. Nanotechnol.* **9**, 218–224 (2014).
12. Roushan, P. et al. Topological surface states protected from backscattering by chiral spin texture. *Nature* **460**, 1106–1109 (2009).
13. Burkov, A. A. & Hawthorn, D. G. Spin and charge transport on the surface of a topological insulator. *Phys. Rev. Lett.* **105**, 066802 (2010).
14. Yazyev, O. V., Moore, J. E. & Louie, S. G. Spin polarization and transport of surface states in the topological insulators Bi_2Se_3 and Bi_2Te_3 from first principles. *Phys. Rev. Lett.* **105**, 266806 (2010).
15. Ando, Y. et al. Electrical detection of the spin polarization due to charge flow in the surface state of the topological insulator $\text{Bi}_{1.5}\text{Sb}_{0.5}\text{Te}_{1.7}\text{Se}_{1.3}$. *Nano Lett.* **14**, 6226–6230 (2014).
16. Edelstein, V. Spin polarization of conduction electrons induced by electric current in two-dimensional asymmetric electron systems. *Solid State Commun.* **73**, 233–235 (1990).
17. Jamali, M. et al. Giant spin pumping and inverse spin hall effect in the presence of surface and bulk spin-orbit coupling of topological insulator Bi_2Se_3 . *Nano Lett.* **15**, 7126–7132 (2015).
18. Han, J. & Liu, L. Topological insulators for efficient spin-orbit torques. *APL Mater.* **9**, 060901 (2021).
19. Fujiwara, K. et al. 5d iridium oxide as a material for spin-current detection. *Nat. Commun.* **4**, 2893 (2013).
20. Mellnik, A. R. et al. Spin-transfer torque generated by a topological insulator. *Nature* **511**, 449–451 (2014).
21. Liu, L. et al. Spin-polarized tunneling study of spin-momentum locking in topological insulators. *Phys. Rev. B* **91**, 235437 (2015).
22. Shiomi, Y. et al. Spin-electricity conversion induced by spin injection into topological insulators. *Phys. Rev. Lett.* **113**, 196601 (2014).
23. Deorani, P. et al. Observation of inverse spin Hall effect in bismuth selenide. *Phys. Rev. B* **90**, 094403 (2014).
24. Lv, Y. et al. Unidirectional spin-Hall and Rashba-Edelstein magnetoresistance in topological insulator-ferromagnet layer heterostructures. *Nat. Commun.* **9**, 111 (2018).
25. Alegria, L. D. et al. Large anomalous Hall effect in ferromagnetic insulator-topological insulator heterostructures. *Appl. Phys. Lett.* **105**, 053512 (2014).
26. Ando, K. et al. Electrically tunable spin injector free from the impedance mismatch problem. *Nat. Mater.* **10**, 655–659 (2011).
27. Brataas, A., Nazarov, Y. V. & Bauer, G. E. W. Finite-element theory of transport in ferromagnet-normal metal systems. *Phys. Rev. Lett.* **84**, 2481–2484 (2000).
28. Zhang, W., Han, W., Jiang, X., Yang, S.-H. & Parkin, S. P. Role of transparency of platinum-ferromagnet interfaces in determining the intrinsic magnitude of the spin Hall effect. *Nat. Phys.* **11**, 496–502 (2015).
29. Panda, S. N., Mondal, S., Sinha, J., Choudhury, S. & Barman, A. All-optical detection of interfacial spin transparency from spin pumping in $\beta\text{-Ta/CoFeB}$ thin films. *Sci. Adv.* **5**, eaav7200 (2019).
30. Panda, S. N. et al. Structural phase-dependent giant interfacial spin transparency in W/CoFeB thin-film heterostructures. *ACS Appl. Mater. Interfaces* **13**, 20875–20884 (2021).
31. Ren, Z., Taskin, A. A., Sasaki, S., Segawa, K. & Ando, Y. Optimizing $\text{Bi}_{2-x}\text{Sb}_x\text{Te}_{3-y}\text{Se}_y$ solid solutions to approach the intrinsic topological insulator regime. *Phys. Rev. B* **84**, 165311 (2011).
32. Bansal, N., Kim, Y. S., Brahlek, M., Edrey, E. & Oh, S. Thickness-independent transport channels in topological insulator Bi_2Se_3 thin films. *Phys. Rev. Lett.* **109**, 116804 (2012).
33. Scanlon, D. O. et al. Controlling bulk conductivity in topological insulators: key role of anti-site defects. *Adv. Mater.* **24**, 2154–2158 (2012).
34. Pandey, A. et al. Pulsed laser deposition of highly c-axis oriented thin films of BSTS topological insulator. <https://arxiv.org/abs/1910.08100> (2019).
35. Lee, J., Park, J., Lee, J.-H., Kim, J. S. & Lee, H.-J. Gate-tuned differentiation of surface-conducting states in $\text{Bi}_{1.5}\text{Sb}_{0.5}\text{Te}_{1.7}\text{Se}_{1.3}$ topological-insulator thin crystals. *Phys. Rev. B* **86**, 245321 (2012).
36. Arakane, T. et al. Tunable Dirac cone in the topological insulator $\text{Bi}_{2-x}\text{Sb}_x\text{Te}_{3-y}\text{Se}_y$. *Nat. Commun.* **3**, 636 (2012).
37. Xu, Y. et al. Observation of topological surface state quantum Hall effect in an intrinsic three-dimensional topological insulator. *Nat. Phys.* **10**, 956–963 (2014).
38. van Kampen, M. et al. All-optical probe of coherent spin waves. *Phys. Rev. Lett.* **88**, 227201 (2002).
39. Mosendz, O. et al. Detection and quantification of inverse spin Hall effect from spin pumping in permalloy/normal metal bilayers. *Phys. Rev. B* **82**, 214403 (2010).
40. Barman, A.; Sinha, J. *Spin dynamics and damping in ferromagnetic thin films and nanostructures*; Springer International Publishing, 2018.
41. Tu, N. H. et al. Large-area and transferred high-quality three-dimensional topological insulator $\text{Bi}_{2-x}\text{Sb}_x\text{Te}_{3-y}\text{Se}_y$ Ultrathin film by catalyst-free physical vapor deposition. *Nano Lett.* **17**, 2354–2360 (2017).
42. Liu, Y., Weinert, M. & Li, L. Spiral growth without dislocations: molecular beam epitaxy of the topological insulator Bi_2Se_3 on Epitaxial Graphene/SiC(0001). *Phys. Rev. Lett.* **108**, 115501 (2012).
43. Orgiani, P. et al. Structural and electronic properties of Bi_2Se_3 topological insulator thin films grown by pulsed laser deposition. *Appl. Phys. Lett.* **110**, 171601 (2017).
44. Liao, Z. et al. Pulsed-laser epitaxy of topological insulator Bi_2Te_3 thin films. *APL Mater.* **7**, 041101 (2019).
45. Tung, Y. et al. Growth and characterization of molecular beam epitaxy-grown $\text{Bi}_2\text{Te}_{3-x}\text{Se}_x$ topological insulator alloys. *J. Appl. Phys.* **119**, 055303 (2016).
46. German, R. et al. Phonon mode calculations and Raman spectroscopy of the bulk-insulating topological insulator BiSbTeSe_2 . *Phys. Rev. Mater.* **3**, 054204 (2019).
47. Yuan, J. et al. Raman Spectroscopy of Two-Dimensional $\text{Bi}_2\text{Te}_x\text{Se}_{3-x}$ Platelets Produced by Solvothermal Method. *Materials* **8**, 5007–5017 (2015).
48. Mukhopadhyay, U. et al. Surface optical and bulk acoustic phonons in the topological insulator, $\text{Bi}_2\text{Se}_2\text{Te}$. *Appl. Phys. Lett.* **106**, 241106 (2015).
49. Gopal, R. K., Singh, S., Mandal, A., Sarkar, J. & Mitra, C. Topological delocalization and tuning of surface channel separation in $\text{Bi}_2\text{Se}_2\text{Te}$ Topological Insulator Thin films. *Sci. Rep.* **7**, 4924 (2017).
50. Garate, I. & Glazman, L. Weak localization and antilocalization in topological insulator thin films with coherent bulk-surface coupling. *Phys. Rev. B* **86**, 035422 (2012).
51. Tserkovnyak, Y., Brataas, A. & Bauer, G. E. W. Enhanced Gilbert Damping in Thin Ferromagnetic Films. *Phys. Rev. Lett.* **88**, 117601 (2002).
52. Tserkovnyak, Y., Brataas, A. & Bauer, G. E. W. Spin pumping and magnetization dynamics in metallic multilayers. *Phys. Rev. B* **66**, 224403 (2002).
53. Tserkovnyak, Y., Brataas, A., Bauer, G. E. W. & Halperin, B. I. Nonlocal magnetization dynamics in ferromagnetic heterostructures. *Rev. Mod. Phys.* **77**, 1375–1421 (2005).
54. Foros, J., Woltersdorf, G., Heinrich, B. & Brataas, A. Scattering of spin current injected in Pd(001). *J. Appl. Phys.* **97**, 10A714 (2005).
55. Kumar, A. et al. Spin transfer torque ferromagnetic resonance induced spin pumping in the Fe/Pd bilayer system. *Phys. Rev. B* **95**, 064406 (2017).
56. Nakayama, H. et al. Geometry dependence on inverse spin Hall effect induced by spin pumping in $\text{Ni}_{81}\text{Fe}_{19}/\text{Pt}$ films. *Phys. Rev. B* **85**, 144408 (2012).
57. Rojas-Sánchez, J.-C. et al. Spin Pumping and Inverse Spin Hall Effect in Platinum: The Essential Role of Spin-Memory Loss at Metallic Interfaces. *Phys. Rev. Lett.* **112**, 106602 (2014).
58. Chen, K. & Zhang, S. Spin pumping in the presence of spin-orbit coupling. *Phys. Rev. Lett.* **114**, 126602 (2015).
59. Hurben, M. J. & Patton, C. E. Theory of two magnon scattering microwave relaxation and ferromagnetic resonance linewidth in magnetic thin films. *J. Appl. Phys.* **83**, 4344–4365 (1998).
60. Arias, R. & Mills, D. L. Extrinsic contributions to the ferromagnetic resonance response of ultrathin films. *Phys. Rev. B* **60**, 7395–7409 (1999).
61. Panda, S. N. et al. Femtosecond laser-induced spin dynamics in single-layer graphene/CoFeB thin films. *Nanoscale* **13**, 13709–13718 (2021).
62. Dutta, K. et al. All-optical detection of spin pumping and giant interfacial spin transparency in $\text{Co}_2\text{Fe}_{0.4}\text{Mn}_{0.6}\text{Si}/\text{Pt}$ Heterostructure. *Adv. Quantum Technol.* **5**, 2200033 (2022).
63. Chen, Y.-T. et al. Theory of spin Hall magnetoresistance. *Phys. Rev. B* **87**, 144411 (2013).
64. Beaurepaire, E., Merle, J.-C., Daunois, A. & Bigot, J.-Y. Ultrafast spin dynamics in ferromagnetic nickel. *Phys. Rev. Lett.* **76**, 4250–4253 (1996).
65. Kittel, C. On the theory of ferromagnetic resonance absorption. *Phys. Rev.* **73**, 155–161 (1948).
66. Katmis, F. et al. A high-temperature ferromagnetic topological insulating phase by proximity coupling. *Nature* **533**, 513–516 (2016).
67. Lang, M. et al. Proximity induced high-temperature magnetic order in topological insulator - ferrimagnetic insulator heterostructure. *Nano Lett.* **14**, 3459–3465 (2014).

68. Zhu, Z. et al. Modulation of magnetic damping in antiferromagnet/CoFeB heterostructures. *Appl. Phys. Lett.* **116**, 182407 (2020).
69. Wu, G., Wu, D., Ren, Y., Jin, Q. Y. & Zhang, Z. Topological surface state manipulation of magnetic damping and surface anisotropy in topological insulator/nonmagnet/CoFe heterostructures. *Phys. Rev. B* **103**, 014419 (2021).
70. Zhang, Y. et al. Crossover of the three-dimensional topological insulator Bi_2Se_3 to the two-dimensional limit. *Nat. Phys.* **6**, 584–588 (2010).
71. Wang, H. et al. Surface-state-dominated spin-charge current conversion in topological-insulator–ferromagnetic-insulator heterostructures. *Phys. Rev. Lett.* **117**, 076601 (2016).
72. Wang, Y. et al. Topological surface states originated spin-orbit torques in Bi_2Se_3 . *Phys. Rev. Lett.* **114**, 257202 (2015).